APL Materials

Cerium reduction at the interface between ceria and yttria-stabilised zirconia and implications for interfacial oxygen non-stoichiometry

Cite as: APL Mater. **2**, 032104 (2014); https://doi.org/10.1063/1.4867556
Submitted: 10 December 2013 . Accepted: 24 February 2014 . Published Online: 06 March 2014

Kepeng Song, Herbert Schmid, Vesna Srot, Elisa Gilardi, Giuliano Gregori, Kui Du, Joachim Maier, and Peter A. van Aken

APL MATERIALS **2**, 032104 (2014)

Cerium reduction at the interface between ceria and yttria-stabilised zirconia and implications for interfacial oxygen non-stoichiometry

Kepeng Song,[1,2] Herbert Schmid,[3] Vesna Srot,[1] Elisa Gilardi,[4] Giuliano Gregori,[4] Kui Du,[2] Joachim Maier,[4] and Peter A. van Aken[1,a]
[1]*Stuttgart Center for Electron Microscopy, Max Planck Institute for Intelligent Systems, Heisenbergstraße 3, 70569 Stuttgart, Germany*
[2]*Shenyang National Laboratory for Materials Science, Institute of Metal Research, Chinese Academy of Sciences, Wenhua Road 72, 110016 Shenyang, China*
[3]*INM-Leibniz Institute for New Materials, Campus D2 2, D-66123 Saarbrücken, Germany*
[4]*Max Planck Institute for Solid State Research, Heisenbergstraße 1, 70569 Stuttgart, Germany*

(Received 10 December 2013; accepted 24 February 2014; published online 6 March 2014)

Epitaxial CeO_2 films with different thickness were grown on Y_2O_3 stabilised Zirconia substrates. Reduction of cerium ions at the interface between CeO_2 films and yttria stabilised zirconia substrates is demonstrated using aberration-corrected scanning transmission electron microscopy combined with electron energy-loss spectroscopy. It is revealed that most of the Ce ions were reduced from Ce^{4+} to Ce^{3+} at the interface region with a decay of several nanometers. Several possibilities of charge compensations are discussed. Irrespective of the details, such local non-stoichiometries are crucial not only for understanding charge transport in such hetero-structures but also for understanding ceria catalytic properties. [http://dx.doi.org/10.1063/1.4867556]

Intermediate temperature solid oxide fuel cells (IT-SOFCs) attract increasing attention since they can provide high energy conversion efficiency at relatively low temperatures (500 °C–700 °C), which would make these devices particularly interesting for practical use.[1–3] Although yttria stabilized zirconia (YSZ) and—particularly at intermediate temperatures—acceptor (e.g., gadolinium, samarium) doped ceria (CeO_2) already provide sufficient ionic conductivity to be employed as SOFC electrolytes, there have been recently strong efforts towards enhancing the oxygen ion transport by combining different materials in multi-layered hetero-structures. Hetero-layers of CaF_2 and BaF_2 have indeed demonstrated enhanced ionic conductivity, which was explained by the space charge theory.[4–6] In recent years, a number of studies have addressed the possibility of enhancing oxygen vacancy conduction through the fabrication of multilayers containing YSZ and/or acceptor doped CeO_2.[7–11] Previous investigations suggested different possible explanations of the interfacial effects such as misfit dislocations, segregations of dopants, strain, and space charge regions.[12,13] However, possible mechanisms for the enhanced ionic conductivity in CeO_2/YSZ hetero-structures are still under discussion. Since interface atomic structures and chemistry are deemed to play crucial roles, it is key to microscopically investigate defined CeO_2/YSZ interfaces, in order to be able to improve the transport properties of these hetero-structured systems.

In the present work, we investigated the model system CeO_2/YSZ (111). Epitaxial CeO_2 films with thickness between 5 nm and 100 nm were prepared on YSZ (111) single crystal substrates with pulsed laser deposition (PLD). The atomic structure of interfaces between CeO_2 thin film and YSZ substrate was then studied by high resolution transmission electron microscopy (HRTEM).

[a]Email: vanaken@is.mpg.de

Oxidation states of cerium were investigated by aberration-corrected STEM combined with spatially resolved electron energy-loss spectroscopy (EELS). The oxidation states of cerium in proximity of the interface were quantitatively determined by comparison of the Ce-$M_{4,5}$ edges acquired from the films with known Ce^{3+} and Ce^{4+} reference edges acquired from $CePO_4$ and CeO_2 standard samples.

Epitaxial CeO_2 thin films with thicknesses ranging from 5 to 100 nm were grown on substrates of YSZ (111) with the dimension of $5 \times 5 \times 0.5$ mm^3 with PLD. An excimer laser with a wavelength of 248 nm (Coherent GmbH, Germany) was employed. The energy density on the target was estimated as 1.5 J cm^{-2}, with a pulse frequency of 5 Hz. The distance between the target and the substrate was 44 mm. During the film deposition, oxygen atmosphere was kept at 0.01 mbar and the temperature at 943 K. After deposition, the films were annealed in the PLD chamber for 30 min in 1 bar oxygen atmosphere at 943 K.

Cross-sectional TEM specimens were prepared by tripod polishing followed by Ar ion thinning with a precision ion polishing system (PIPS, Gatan, model 691) under liquid nitrogen cooling to achieve electron transparency. HRTEM observations were performed at 400 kV on a JEOL-4000FX (JEOL, Tokyo, Japan) microscope. STEM and EELS measurements were carried out on an advanced analytical TEM/STEM (JEOL-ARM200CF, JEOL Co. Ltd) at 200 kV equipped with a cold field emission gun and a probe Cs-corrector (CEOS Co. Ltd.). High-angle annular dark-field (HAADF)-STEM images were taken at a convergence semi-angle of 25 mrad which provided a probe size of about 0.1 nm. Data on oxidation-state sensitive Ce-$M_{4,5}$ energy-loss near-edge structures (ELNES) were obtained by acquiring EELS line-scans (1 dimensional (1D) spectrum images) with a post-column energy filter (Gatan GIF Quantum ER with high-speed dual-EELS functions; Gatan Inc. Pleasanton, USA) in STEM mode. HAADF and EELS signals were simultaneously collected and reference regions in the HAADF-STEM images were used for spatial drift correction.

Both CeO_2 and YSZ crystallize in the CaF_2-type fluorite structure (space group: Fm3m; a_{CeO_2} = 0.541 nm, a_{YSZ} = 0.514 nm). Figure 1(a) is a low magnification bright-field STEM image indicating that the CeO_2 film has a continuous morphology with a thickness of about 100 nm. Selected area electron diffraction (SAED) patterns showed a cube-on-cube orientation relationship ($\langle$1-10$\rangle$ $(111)_{CeO_2}$//$\langle$1-10$\rangle$ $(111)_{YSZ}$) between the CeO_2 film and the YSZ substrate (Figure 1(b)). Figure 1(c) shows a typical cross-section viewed HRTEM image of the CeO_2/YSZ (111) interface, in which the interface position is indicated by an arrow. Neither amorphous nor secondary phase precipitates are present at the interface, while the CeO_2 crystal preserves its cubic lattice. Periodically spaced misfit dislocations associated with an extra (11-1) atomic plane in the YSZ side are clearly distinguishable along the interface, and are separated by approximately 6.9 nm every 22nd–23rd atomic planes in average spacing, which approximately agrees with the expected value (every 19th atomic planes) calculated from the lattice mismatch ($\Delta f = (a_{CeO_2}\text{-}a_{YSZ})/a_{YSZ} = 5.3\%$). This means that the lattice mismatch is almost completely relaxed by the misfit dislocations; yet a small compressive strain remains present in the CeO_2 film between two dislocations. However, it is important to note that in the core region of the dislocations (on the CeO_2 side of the interface), the strain field is tensile, as shown by the distorted lattice planes. Burgers circuit was drawn to characterize the projected Burgers vector **b** for the misfit dislocations at the interface (Inset (d) in Figure 1). The Burgers vector of the misfit dislocations is parallel to the interface, thus it should be **a**/2$\langle$10-1$\rangle$ or **a**/2$\langle$01-1$\rangle$. In order to investigate the chemistry of CeO_2 at the interfacial region, series of EEL spectra were acquired with a probe size of about 0.1 nm by line-scans across the CeO_2/YSZ interface. The Ce-$M_{4,5}$ edges reflect electronic transitions from 3d to 4f states (M_4 corresponds to the $3d_{3/2}$ to $4f_{5/2}$ transition and M_5 to the $3d_{5/2}$ to $4f_{7/2}$ transition) combining with ligand hole effects.[14] The Ce-$M_{4,5}$ ELNES are valence sensitive, which can be utilized to obtain spatially resolved chemical information of Ce-containing materials.[15,16] Figure 2 shows reference spectra acquired from pure CeO_2 and $CePO_4$, in which Ce-ions have pure valences of 4+ and 3+, respectively. The characteristic differences in these spectra provide a basis for the following quantitative analysis of experimental EELS data.

Results of EELS line-scans across the CeO_2/YSZ interface are shown in Figure 3. A 1D spectrum image (SI) was acquired along the profiles as indicated in the high-angle annular dark-field STEM (HAADF-STEM) image (Figure 3(a)). Two line-scan analyses were conducted across the interface as shown in Figure 3(a)—line-scan 01 (LS01) across the region between two misfit dislocations under weak compressive strain and line-scan 02 (LS02) across the misfit dislocation core (under

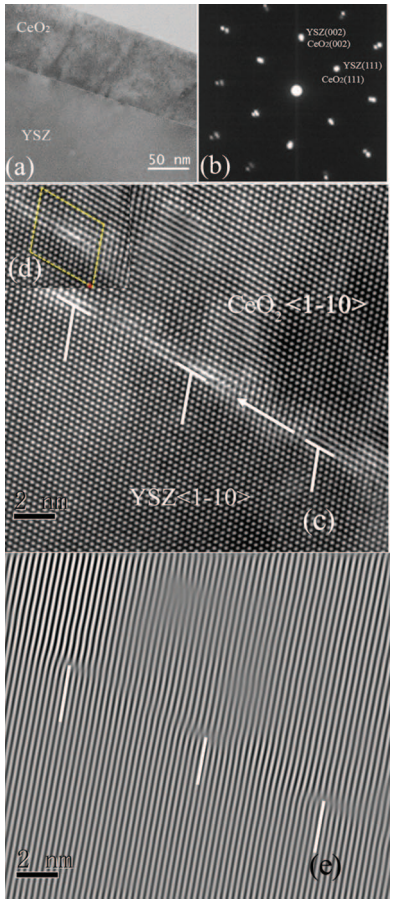

FIG. 1. Morphology of the film shown by the low magnification bright-field STEM image (a) and orientation relationship revealed by selected area electron diffraction patterns from zone axis $\langle 1\text{-}10\rangle_{YSZ}$ (b). Figure (c) is the HRTEM micrograph of the CeO_2/YSZ (111) interface viewed from the $[1\text{-}10]_{YSZ}$ direction; the position of the interface is indicated by the arrow. Inset (d) displays a detail of the interface showing the Burgers circuit of the misfit dislocations. (e) Fourier-filtered image of (c) showing the misfit dislocations.

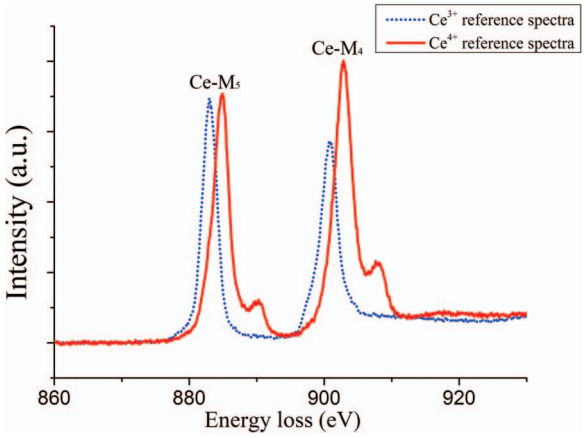

FIG. 2. Reference energy-loss near-edge structures (ELNES) acquired from standard samples—$CePO_4$ (representing Ce^{3+}) and CeO_2 (representing Ce^{4+}).

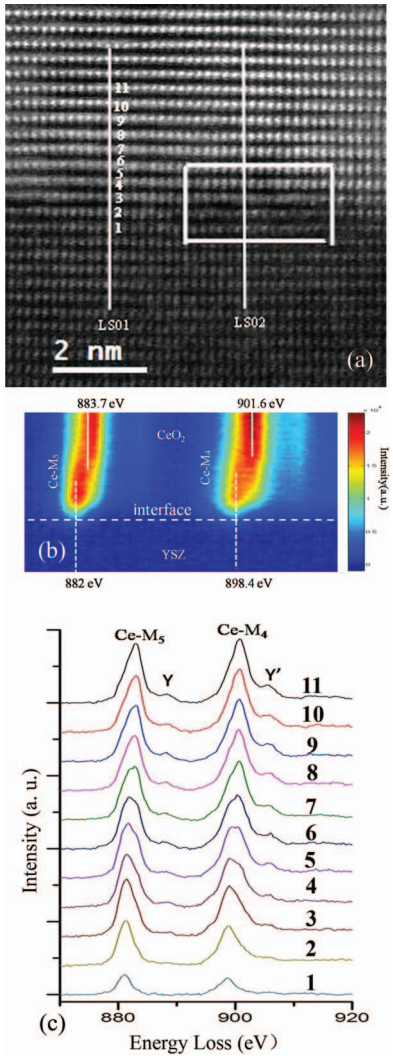

FIG. 3. (a) Schematic HAADF-STEM image showing the position of the EELS line scans across the CeO_2/YSZ (111) interface. Line-scan 01 (LS01) went across regions between misfit dislocations and line-scan 02 (LS02) across the misfit dislocation core. (b) EELS spectrum image from LS01. (c) EELS spectra extracted from the spectrum image acquired along LS01, which illustrate the change of Ce-$M_{4,5}$ edge from the bulk to the interface.

tensile strain). In this incident direction (⟨-1-12⟩), the dislocation line was inclined 30° with respect to the electron beam. The dislocation core region was then judged by the incoherent area which corresponds to the projection of the dislocation line. Spectrum image of the Ce-$M_{4,5}$ edges from LS01 is shown in Figure 3(b). From this, it can be recognized that the Ce-$M_{4,5}$ edges from areas immediately adjacent to the interface exhibit an evident shift towards lower energies compared with the bulk region further away from the interface. To qualitatively elucidate the changes of the cerium valence between different scan positions, EEL spectra (displayed in Figure 3(c) after background subtraction) were extracted from the SI. Significant changes of the Ce-$M_{4,5}$ edges from bulk CeO_2 to the interface can be discerned: (i) A higher intensity ratio (>1) of the Ce-M_5/Ce-M_4 is observed in proximity of the interface, whereas it is inversed in regions further away from the interface. (ii) Both Ce-M_5 and Ce-M_4 edges shift to the lower energy side from the bulk region towards the interface. (iii) The intensities of the peaks Y and Y′ on the shoulder beyond the Ce-M_5 and Ce-M_4 decrease from the bulk region to the interface.[17] Comparing these spectra with the reference EEL spectra for Ce^{4+} and Ce^{3+}, it is obvious that contributions from Ce^{4+} ions dominate the Ce-$M_{4,5}$ edges in the CeO_2 bulk region, while those close to the interface indicate increased contributions from Ce^{3+}

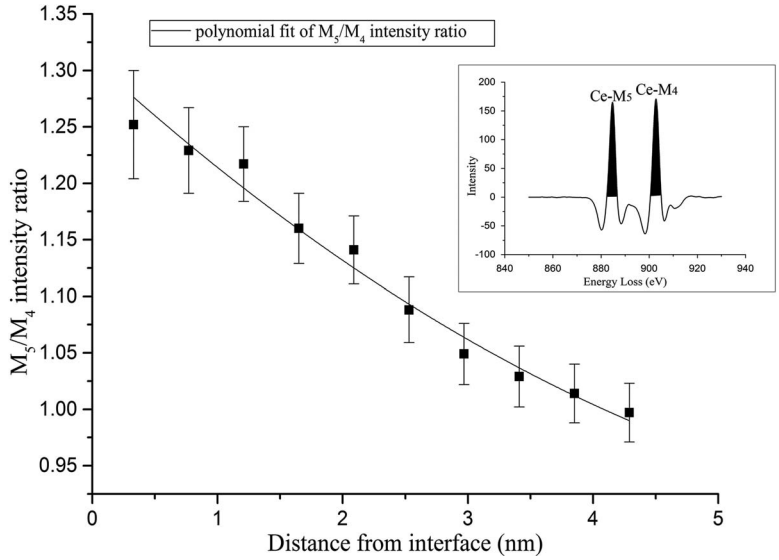

FIG. 4. Plot of the Ce-M_5/M_4 edges intensity ratio based on the second derivative method. The inset shows the spectra obtained by 2nd derivative method.

ions. Previous research showed that the Ce-M_5/Ce-M_4 intensity ratio in second derivative spectra is insensitive to energy resolution and sample thickness in the regime of $\Delta E < 1$ eV and $t/\lambda < 1$ (ΔE is energy resolution here, and t is thickness, λ is inelastic electron mean free path).[17] The oxidation state of the Ce ions was quantitatively analyzed by calculating the Ce-M_5/Ce-M_4 intensity ratios with the positive part of second derivative of the extracted spectra, as shown in Figure 4 (the second derivative spectra is plotted in the inset in Figure 4). This method yields the Ce-M_5/Ce-M_4 intensity ratio of about 0.93 for Ce^{4+} and 1.25 for Ce^{3+} in pure standards.[18–20] Figure 4 clearly reveals that the Ce-M_5/Ce-M_4 ratio is about 1.25 at the interface, while it is gradually decreasing to 0.98 in the bulk area at a distance of about 4.3 nm away from the interface. Based on these results, it is concluded that the Ce^{4+} ions are dominant in bulk CeO_2 regions while those at the interfacial regions tending to be reduced to Ce^{3+}.

Another important result is given by the comparison of the spectra collected at the film/substrate interface along line-scan LS01 (weak compressive strain) and LS02 (tensile strain). This data (together with a spectrum acquired from a partially relaxed 5 nm thick film) are shown in Figure 5. Remarkably, the 3 spectra exhibit identical Ce-M_5/M_4 intensity ratios (within the experimental error), meaning that the high Ce^{3+} concentration at the interface does not depend on the strain field.

To quantitatively determine the reduction extent, i.e., the Ce^{3+}/Ce^{4+} ratio, a multiple linear least squares (MLLS) fitting method was employed to calculate the Ce^{3+} fraction.[11,21] Spectra acquired from CeO_2 and $CePO_4$ powders were used as reference spectra for Ce^{4+} and Ce^{3+}, respectively. All the spectra were normalized based on the integrated intensity of continuum background in the range between 915 eV and 925 eV (after background subtraction and removal of plural scattering). With this method, all the extracted spectra could be reproduced by the weighted sum of the two reference spectra. In this way, the integrated area under the Ce-$M_{4,5}$ edges quantitatively reflect the ratio of the occupancy of f-holes. Based on this method, the Ce^{3+} fraction for different position was calculated and plotted as function of distance from the interface as shown in Figure 6. Analogous Ce^{3+} profiles were obtained also across the interfaces for thinner films (5 nm and 30 nm). The calculations indicate a prevalence of about completely Ce^{3+} ions at the interface while this fraction decreases to about 25% in the bulk region, which is about 4.3 nm away from the interface. The error bars correspond to the standard deviation between experimental and fitting spectra. From these results, it is revealed that the present CeO_2/YSZ interface region is nonstoichiometric with a high concentration of Ce^{3+} ions close to the interface, despite which the fluorite structure is maintained.

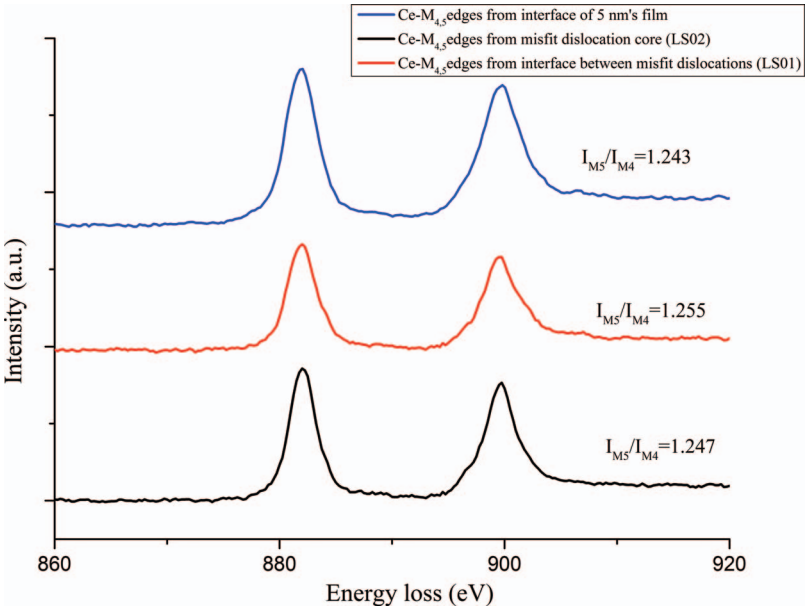

FIG. 5. Ce-$M_{4,5}$ edges and corresponding intensity ratios from strain-relaxed region (red) between 2 dislocations, misfit dislocation core (black) and partially relaxed 5 nm thick CeO_2 film (blue).

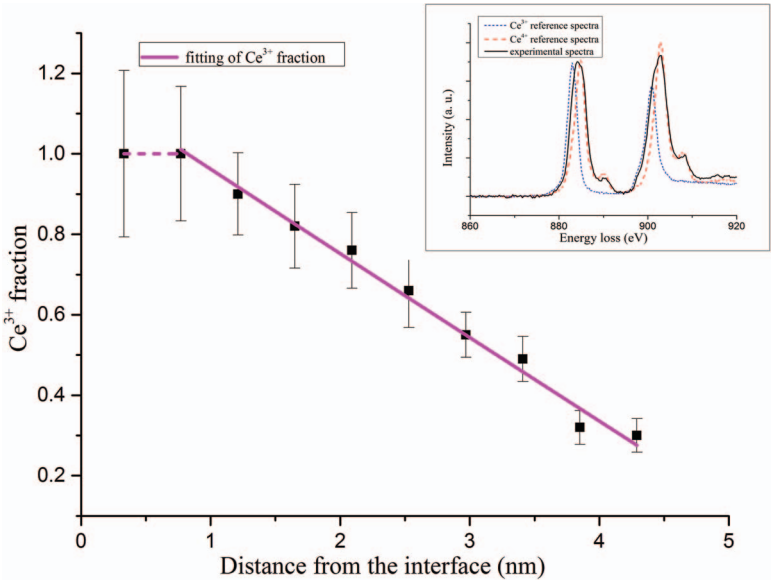

FIG. 6. Ce^{3+} fraction vs. distance from interface calculated by the multiple linear least squares method. The inset illustrates the multiple linear least squares fitting method.

Importantly, no diffusion of yttrium into CeO_2 was detected by line-scans across the interface via energy-dispersive X-ray spectroscopy (EDS). The large Ce^{3+} concentration in proximity of the interface (see Figure 6) corresponds to an increased n-type conductivity; however, the profile is also of direct relevance for ionic effects. There are at least 3 possibilities of how Ce^{3+} is charge compensated; they distinguish themselves by the location of the oxygen vacancies: (1) in CeO_2, (2) in the interfacial core, or (3) in YSZ. If a neutral interface (case 1) is assumed and the local electroneutrality condition $[Ce'_{Ce}] = 2[V_O^{\cdot\cdot}]$ is invoked, one expects an accumulation of oxygen vacancies at the interface following the Ce^{3+} fraction increase. Interestingly, the reduction of Ce^{4+} to Ce^{3+} is usually accompanied by the local expansion of the lattice.[22,23] Similarly, recent density functional

theory calculations performed on a CeO_2/ZrO_2 junction, predicted lower oxygen vacancy formation energy at the interface (due to the strain state) than in the bulk (from 2.80 eV in bulk to 0.50 eV at the interfacial plane of CeO_2).[24] Nonetheless, as shown in Figure 5, the Ce-M_5/M_4 intensity ratios collected from regions of the sample with different strain fields (compressive vs. tensile) as well as from a partially strain-relaxed 5 nm thick film are identical. This suggests that misfit strain is not the predominant factor in determining the Ce^{3+} enrichment at the interface.

As previously pointed out, electro-neutral interfaces are a very special case.[23] The fact that the Ce^{3+} fraction profile extends up to 4.3 nm (according to our line-scan scope) suggests that other effects may come into play and affect the spatial distribution of charged defects (including oxygen vacancies) near the interface such as space charge effects. It is worth noting that in proximity of a charged interface an increasing trivalent cerium concentration would correspond to a decreasing oxygen vacancies concentration in the ceria environment. Interestingly, the observed extent of the Ce^{3+} fraction profile is consistent with the expected size of space charge regions in nominally un-doped ceria. The shape of the profiles (Figure 6) is not consistent with defect concentrations relying on the Boltzmann statistics (diluted systems). At a first glance, the profile appears to be almost linear. Yet, a better approximation is increasing profiles that saturate at the boundary. Indeed, a Fermi-Dirac distribution taking the exhaustion of available sites due to the large concentration of defects into account would describe the observed profiles more appropriately and in particular the Ce^{3+} saturation occurring at distances <1 nm. It is worth noting that for global electro-neutrality reasons such an excess negative charge $[Ce'_{Ce}]$ on the ceria side requires an excess positive charge, which can be located (case 2) in the interface core or (case 3) at the YSZ side of the interface. For electrostatic reasons this would go along—in both cases—with an oxygen depletion in the space charge zone of CeO_2, which is important as far as ion transport is concerned. Case 2 holds for the grain boundaries of several polycrystalline ceramics (including YSZ and CeO_2) and relies on the presence of structurally necessary oxygen vacancies, which accommodate the orientation mismatch between adjacent grains. In the CeO_2/YSZ interface, oxygen vacancies could then be expected to segregate in the misfit dislocation cores and to give rise to the excess positive charge, in an analogous manner to what was already observed for $SrTiO_3$ bicrystals with low-angle tilt.[25]

Otherwise in case 3, the compensating positive charge stems from an excess oxygen vacancy concentration on the YSZ side of the interface. Unfortunately, EELS analysis did not provide conclusive evidences regarding the spatial distribution of the oxygen vacancies at the interface. Finally, as regions with different strain fields exhibit identical Ce-M_5/M_4 intensity ratios (i.e., identical Ce^{3+} concentrations), strain effects alone are not the only cause of the cerium reduction at the interface. Rather also the presence of space charge effects needs to be taken into account. This would be in line with both extent and shape of the Ce^{3+} profile (see Figure 6).

In summary, the local microstructure and chemistry of the CeO_2/YSZ (111) interface have been investigated by means of HRTEM and STEM techniques. Periodically distributed misfit dislocations were observed in the YSZ substrate along the interface. STEM-EELS analysis reveals an interface region with a high fraction of Ce^{3+}. This finding is extremely relevant for the transport behavior, in particular because the Ce^{3+} should be homogeneously or heterogeneously charge compensated by oxygen vacancies.[26] Moreover, the varied local defect chemistry is relevant also for redox and acid-base effects in catalysis.[27]

The authors thank U. Salzberger for the TEM sample preparation. Professor E. Arzt is greatly acknowledged for his continuous support with the STEM project through INM-Leibniz Institute for New Materials. K.S. acknowledges the financial support from the Ph.D. student exchange program between the Max-Planck Society and the Chinese Academy of Sciences and the Natural Sciences Foundation of China (Grant No. 51221264). The research leading to these results has received funding from the European Union Seventh Framework Program [FP/2007-2013] under Grant Agreement No. 312483 (ESTEEM2).

[1] J. B. Goodenough, Nature (London) **404**, 821 (2000).
[2] S. P. S. Badwal, Solid State Ionics **52**, 23 (1992).
[3] V. Esposito and E. Traversa, J. Am. Ceram. Soc. **91**, 1037 (2008).
[4] N. Sata, K. Ebenman, K. Ebert, and J. Maier, Nature (London) **408**, 946 (2000).

[5] X. Guo, I. Matei, J. Jamnik, J. Lee, and J. Maier, Phys. Rev. B **76**, 125429 (2007).
[6] X. Guo and J. Maier, Adv. Mater. **21**, 2619 (2009).
[7] S. Azad, O. A. Marina, C. M. Wang, L. Saraf, V. Shutthanandan, D. E. McCready, A. El-Azab, J. E. Jaffe, M. H. Engelhard, C. H. F. Peden, and S. Thevuthasan, Appl. Phys. Lett. **86**, 131906 (2005).
[8] A. Peters, C. Korte, D. Hesse, N. Zakharov, and J. Janek, Solid State Ionics **178**, 67 (2007).
[9] C. Korte, A. Peters, J. Janek, D. Hesse, and N. Zakharov, Phys. Chem. Chem. Phys. **10**, 4623 (2008).
[10] N. Schichtel, C. Korte, D. Hesse, and J. Janek, Phys. Chem. Chem. Phys. **11**, 3043 (2009).
[11] D. Pergolesi, E. Fabbri, S. N. Cook, V. Roddatis, E. Traversa, and J. A. Kilner, ACS Nano **6**, 10524 (2012).
[12] E. Fabbri, D. Pergolesi, and E. Traversa, Sci. Technol. Adv. Mater. **11**, 054503 (2010).
[13] M. C. Göbel, G. Gregori, X. Guo, and J. Maier, Phys. Chem. Chem. Phys. **12**, 14351 (2010).
[14] H. Dexpert, R. C. Karnatak, J. M. Esteva, J. P. Connerade, M. Gasgnier, P. E. Caro, and L. Albert, Phys. Rev. B **36**, 1750 (1987).
[15] A. Kotani and H. Ogasawara, J. Electron Spectrosc. Relat. Phenom. **60**, 257 (1992).
[16] L. A. J. Garvie and P. R. Buseck, J. Phys. Chem. Solids **60**, 1943 (1999).
[17] J. A. Fortner and E. C. Buck, Appl. Phys. Lett. **68**, 3817 (1996).
[18] H. Hojo, T. Mizoguchi, H. Ohta, S. D. Findlay, N. Shibata, T. Yamamoto, and Y. Ikuhara, Nano Lett. **10**, 4668 (2010).
[19] P. Yan, T. Mori, Y. Wu, Z. Li, G. J. Auchterlonie, J. Zou, and J. Drenman, Microsc. Microanal. **19**, 102 (2013).
[20] J. M. Perkins, S. Fearn, S. N. Cook, R. Srinivasan, C. M. Rouleau, H. M. Christen, G. D. West, R. J. H. Morris, H. L. Fraser, S. J. Skinner, J. A. Kilner, and D. W. McComb, Adv. Funct. Mater. **20**, 2664 (2010).
[21] S. Turner, S. Lazar, B. Freitag, R. Egoavil, J. Verbeeck, S. Put, Y. Strauven, and G. V. Tendeloo, Nanoscale **3**, 3385 (2011).
[22] S. Deshpande, S. Patil, S. V. N. T. Kuchibhatla, and S. Seal, Appl. Phys. Lett. **87**, 133113 (2005).
[23] A. Kossoy, Y. Feldman, E. Wachtel, K. Gartsman, I. Lubomirsky, J. Fleiq, and J. Marier, Phys. Chem. Chem. Phys. **8**, 1111 (2006).
[24] M. Fronzi, S. Cereda, Y. Tateyama, A. D. Vita, and E. Traversa, Phys. Rev. B **86**, 085407 (2012).
[25] R. A. D. Souza, J. Fleig, J. Maier, O. Kienzle, Z. Zhang, W. Sigle, and M. Ruhle, J. Am. Ceram. Soc. **86**, 922 (2003).
[26] Q. Su, D. Yooh, A. Chen, F. Khatkhatay, A. Manthiram, and H. Wang, J. Power Sources **242**, 455 (2013).
[27] R. Merkle and J. Maier, Top. Catal. **38**, 141 (2006).